


Article

Synthesis and Characterization of Bismuth-Cerium Oxides for the Catalytic Oxidation of Diesel Soot

Sabrina C. Hebert and Klaus Stöwe * 

Faculty of Natural Science, Professorship of Chemical Technology, Chemnitz University of Technology, 09111 Chemnitz, Germany; sabrina-christina.hebert@chemie.tu-chemnitz.de

* Correspondence: klaus.stöwe@chemie.tu-chemnitz.de

Received: 28 February 2020; Accepted: 16 March 2020; Published: 18 March 2020



Abstract: In this paper, the syntheses of a set of cerium-bismuth mixed oxides with the formula $Ce_{1-x}Bi_xO_{2-x/2}$, where the range of x is 0.0 to 1.0 in 10 mol% steps, via co-precipitation methods is described. Two synthesis routes are tested: The “normal” and the so called “reverse strike” (RS) co-precipitation route. The syntheses are performed with an automated synthesis robot. The activity for Diesel soot oxidation is measured by temperature programmed oxidation with an automated, serial thermogravimetric and differential scanning calorimetry system (TGA/DSC). P90 is used as a model soot. An automated and reproducible tight contact between soot and catalyst is used. The synthesized catalysts are characterized in terms of the specific surface area according to Brunauer, Emmett and Teller (S_{BET}), as well as the dynamic oxygen storage capacity (OSC_{dyn}). The crystalline phases of the catalysts are analysed by powder X-ray diffraction (PXRD) and Raman spectroscopy. The elemental mass fraction of the synthesized catalysts is verified by X-ray fluorescence (XRF) analysis. A correlation between the T_{50} values, OSC_{dyn} and S_{BET} has been discovered. The best catalytic performance is exhibited by the catalyst with the formula RS- $Ce_{0.8}Bi_{0.2}O_x$ which is synthesized by the reverse strike co-precipitation route. Here, a correlation between activity, OSC_{dyn} , and S_{BET} can be confirmed based on structural properties.

Keywords: bismuth-cerium-oxides; co-precipitation; reverse strike precipitation; diesel soot oxidation; dynamic oxygen storage capacity

1. Introduction

Diesel soot has proven to be carcinogenic [1] and furthermore, it can influence the environment, the vegetation, or the climate [2]. Diesel soot may cause lung or cardiovascular diseases [3,4]. Therefore, different technologies to control the emission of Diesel soot have been developed. Modern Diesel vehicles possess a Diesel particulate filter (DPF) system to filtrate Diesel soot from the exhaust stream. Over time, Diesel soot accumulates on the surface or in the channels of the DPF. The accumulated Diesel soot causes an increase in pressure drop, and this influences the fuel consumption or leads to filter failure [2]. In the absence of a filter regeneration process, the car engine will stop due to DPF plugging [5]. Today, active and passive regeneration processes are established. Another possibility is the use of fuel born catalysts based on Ce or Fe [6]. During the active regeneration process, the accumulated soot is periodically combusted in an oxidising atmosphere when the pressure drop reaches a preset limit. The heat for this process is generated by an electric heater, a flame-based burner, or microwave cavity [7]. At the active regeneration process, temperatures above 600 °C are reached. This causes on the one hand problems with materials of the DPF because of their melting point [8]. On the other hand, large amounts of energy are needed [9]. Therefore, the filter wall is coated with a catalyst [2]. During the passive regeneration, the accumulated soot is combusted continuously by chemical reaction. Here, no additional amount of fuel is needed and the oxidation temperature is equal

to the exhaust temperature. The problem of the passive regeneration is the suitability and costs of catalysts. Common catalysts are based on precious metals [2].

Many researchers investigate soot oxidation with ceria as catalyst applied in three-way catalytic converters, in solid oxide fuel cells fed with hydrocarbons, or in the water-gas-shift reaction [10]. Ceria has the ability to incorporate oxygen vacancies into the lattice resulting in a substoichiometric phase CeO_{2-x} through a reduction process [11]. The $\text{Ce}_{1-x}\text{Bi}_x\text{O}_{2-x/2}$ -system is a promising candidate for the passive regeneration of the DPF [12]. This mixed oxide system is free of precious metals. The investigation of this system is directly related to the introduction of vacancies in oxide ion sublattice. Oxide ion vacancies are inherent to ceria. Additionally, doping with ions with a lower formal charge than in Ce^{4+} and an asymmetric coordination sphere like Bi^{3+} ions increases the amount of oxide ion vacancies and reducibility of the oxide. Via s-p-hybridisation in the formal electron configuration of Bi^{3+} $[\text{Xe}] 4f^{14}5d^{10}6s^26p^0$ the coordination sphere of this ion is typically distorted (so-called lone pair) [10]. Dikmen et al. observed a high oxide ion conductivity for Bi-doped CeO_2 . They synthesized Bi-Ce mixed oxides via co-precipitation and subsequent hydrothermal aging at $T = 900 - 1300$ °C [13]. Zhao and Feng doped CeO_2 with Bi^{3+} and M^{2+} ($\text{M} = \text{Ca}^{2+}, \text{Sr}^{2+}, \text{Ba}^{2+}$). All of their synthesized oxides possess a high oxide ion conductivity. The highest oxide ion conductivity showed the following oxide: $\text{Ce}_{0.95}\text{Ca}_{0.05}\text{Bi}_{0.4}\text{O}_{2.55}$ [14]. Hund et al. synthesized Bi^{3+} -doped CeO_2 via solid state reaction at $T = 800$ °C. They found up to 40 mol% Bi^{3+} exclusively as fluorite-type CeO_2 crystalline phase but with increased lattice constant of the cubic mixed oxide phase because of Bi^{3+} insertion [15]. A more detailed investigation of the crystal structure of Bi^{3+} -doped CeO_2 has not yet been made. This is because all the prepared Bi-Ce mixed oxides have nanocrystalline structures [10] and these reveal very broad reflections in PXRD pattern. First attempts to clarify the structure are made with the combination of extended X-ray absorption fine structure (EXAFS) and PXRD by Frolova et al. They discovered that the introduction of bismuth oxide in CeO_2 leads to the formation of a single-phase solid solution system. The resulting structure is close to the fluorite-type structure of CeO_2 . With increasing Bi content, the unit cell parameter and the disorder of the structure increases [16]. Sardar et al. synthesized mixed oxides via hydrothermal synthesis starting from cerium chloride and sodium bismutate at $T = 240$ °C. They investigated the structure through XRD and X-ray absorption near-edge fine structure (XANES) measurements. They conclude that the mixed oxides have the formula $\text{Ce}_{1-x}^{4+}\text{Bi}_x^{3+}\text{O}_{2-0.5x}$ ($x \leq 0.6$) and reveal a locally distorted fluorite-type structure because of the unsymmetrical coordination of Bi^{3+} [10].

In this paper, a series of Bi-Ce mixed oxides with varying molar ratio between Ce and Bi are synthesized automatically via the synthesis robot Chemspeed Accelerator SLT 106. Two routes of co-precipitation are used: The normal co-precipitation route and the reverse strike co-precipitation route according to Lee et al. [17]. In the normal co-precipitation route, the precipitation agent is added to the metal salt precursor solution. The reaction runs from low to high pH values. Due to hydrolysis reactions, we have to deal with different beginnings of precipitation for different precursors. For the reverse strike co-precipitation route, the premixed precursor solution is added to the precipitation agent. Thus, the reaction starts in the basic pH range and ends at $\text{pH} = 6$. This method guarantees a homogenous start of the precipitation and prevents the oligomerisations of hydrated bismuth oxides in the acidic pH range [17,18]. The catalysts are characterized via PXRD, Raman spectroscopy, X-ray fluorescence (XRF), and specific surface measurements according to Brunauer, Emmett, and Teller (S_{BET}). The catalytic activity for Diesel soot oxidation and dynamic oxygen storage capacity (OSC_{dyn}) are measured by automated serial thermogravimetric analysis methods.

2. Materials and Methods

2.1. Catalyst Preparation

The chemicals specified below were used without any further purification.

A set of cerium-bismuth mixed oxides with the formula $\text{Ce}_{1-x}\text{Bi}_x\text{O}_{2-x/2}$ in the range of $0.0 \leq x \leq 1.0$ in 10 mol% steps were prepared via co-precipitation methods. The syntheses were performed

with the synthesis robot Accelerator SLT106 from Chemspeed Technologies AG, Switzerland. Two co-precipitation synthesis routes were used: The normal co-precipitation with continuous addition of the precipitation agent via a 4-needle head (4NH) of the synthesis robot for liquid dosing to a given solution mixture of both metal salts and the reverse strike co-precipitation route according to Lee et al. [17] with reversal of this sequence of solution combination. The syntheses were performed in lined beakers with magnetic stirring bars, which were tempered via a thermostat from Huber Corp. to a temperature of $T = 25\text{ }^{\circ}\text{C}$. The control of the thermostat was implemented in the software “ApplicationExecutor” for the synthesis robot. During the normal co-precipitation route, 0.5 M $\text{Ce}(\text{NO}_3)_3 \cdot 6\text{H}_2\text{O}$ and 0.5 M $\text{Bi}(\text{NO}_3)_3 \cdot 5\text{H}_2\text{O}$ (99.5%, Alfa Aesar) were dissolved in 1 M HNO_3 and transferred in beakers as reservoirs. Via the 4NH of the synthesis robot, the corresponding molar amounts of the solutions were pipetted into lined beakers, mixed by magnetic stirring and kept at $T = 25\text{ }^{\circ}\text{C}$. In a different lined beaker the precipitant, in our case a 1 M $(\text{NH}_4)_2\text{CO}_3$ (food grade, BASF) solution, which was dissolved in ultra-pure water, was also brought to a temperature $T = 25\text{ }^{\circ}\text{C}$. Via 4NH, the precipitant was transferred to the premixed nitrate solutions. The white to pale yellow precipitations were stirred for a further $t = 0.5\text{ h}$ at $T = 25\text{ }^{\circ}\text{C}$. After stirring, the precipitations were separated from the supernatants via a 3-fold parallel pressure filtration station at an overpressure of $p = 1\text{ bar}$. Polyethersulfone membranes (Sartorius Stedim Biotech Corp.) with $0.1\text{ }\mu\text{m}$ mean pore size were used for filtration. The filtrated samples were dried over night at room temperature, crushed and ground in an agate mortar until fine powders were received and subsequently calcined at $T = 800\text{ }^{\circ}\text{C}$ for $t = 5\text{ h}$. During the reverse strike co-precipitation route the corresponding molar amounts of the nitrates were premixed. The premixed nitrate solution was continuously dosed via the 4NH to the tempered precipitant until a preset pH was achieved ($\text{pH} = 6$). The subsequent downstream processes of stirring, filtration, and calcination were equal to the normal co-precipitation route. The dispensing and aspirating speeds are summarized in Table 1.

Table 1. Dispensing and aspirating speeds of the pipetting steps. The 4-needle head (4NH) of the synthesis robot Chemspeed Accelerator SLT106 is used for liquid dosing.

Solution	Dispensing Speed [$\text{mL}\cdot\text{min}^{-1}$]	Aspirating Speed [$\text{mL}\cdot\text{min}^{-1}$]
0.5 M $\text{Ce}(\text{NO}_3)_3 \cdot 6\text{H}_2\text{O}$	40	40
0.5 M $\text{Bi}(\text{NO}_3)_3 \cdot 5\text{H}_2\text{O}$	40	40
premixed nitrate solution	40	40
1 M $(\text{NH}_4)_2\text{CO}_3$	40	80

2.2. Activity Measurements—Soot Oxidation and OSC_{dyn}

The catalytic performance for soot oxidation of the synthesized catalysts was investigated by automated serial thermogravimetric analyses coupled with heat flow differential scanning calorimetry (TGA-DSC 1 1600; Mettler Toledo Corp.). The model soot used was the carbon black P90 supplied by Evonik Degussa. In this work, the so-called tight contact in an automated mode was used. The tight contact was realized with an asymmetric dual centrifuge in a highly reproducible mode of operation. For this purpose, the SpeedmixerTM from Hauschild Corp. was used. The soot and catalyst with a weight ratio of 1:4 were mixed for $t = 300\text{ s}$ at a rotation speed of $rs = 3000\text{ rpm}$. Ca. $m = 10\text{ mg}$ of the mixed soot and catalyst was placed in a corundum crucible of volume $V = 70\text{ }\mu\text{l}$ and heated to $T = 700\text{ }^{\circ}\text{C}$ at a heating rate of $r = 5\text{ }^{\circ}\text{C}\cdot\text{min}^{-1}$ with a synthetic air flow of $\dot{V} = 25\text{ mL}\cdot\text{min}^{-1}$. The activity of the catalyst was determined by the characteristic combustion temperature at a specific weight loss. In this work, the T_{50} temperatures were used. These were the temperatures where 50% of the soot was oxidized. These values were determined with the help of software Star^e from Mettler Toledo Corp.

Another significant property for soot oxidation catalysts is the dynamic oxygen storage capacity (OSC_{dyn}). In this work, OSC_{dyn} was determined with the help of the TGA-DSC11600 from Mettler Toledo Corp., described above. To calculate the OSC_{dyn} , two heating and cooling cycles were performed.

First, $m = 30$ mg of the catalyst which was calcined at $T = 800$ °C was placed in a $V = 70$ μ l corundum crucible and heated to $T = 700$ °C under a nitrogen flow of $\dot{V} = 25$ mL \cdot min $^{-1}$ to release adsorbed oxygen, water, or other compounds. The system was stabilized for $t = 10$ min. Next, the system was cooled to $T = 150$ °C under a synthetic air flow of $\dot{V} = 25$ mL \cdot min $^{-1}$ for oxygen uptake and stabilized for $t = 10$ min. This procedure was repeated and the weight loss of the second heating step was used for calculating the OSC_{dyn} as mass difference of $\frac{m_{O_2}^{150\text{ }^\circ\text{C}} - m_{N_2}^{700\text{ }^\circ\text{C}}}{M_{O_2} \cdot m_{cat}}$, where $m_{O_2}^{150\text{ }^\circ\text{C}}$ is the mass of catalyst at a temperature $T = 150$ °C after oxygen uptake, $m_{N_2}^{700\text{ }^\circ\text{C}}$ is the mass of catalyst at $T = 700$ °C after oxygen release, M_{O_2} is the molar mass of oxygen, and m_{cat} is the buoyancy-corrected mass of catalyst weighed in a $V = 70$ μ l corundum crucible after desorption of compounds like water. OSC_{dyn} is represented in $\mu\text{mol}_{O_2} \cdot \text{g}_{cat}^{-1}$. For measuring the OSC_{dyn} a heating/cooling rate of $r = 5$ °C \cdot min $^{-1}$ was used.

2.3. Catalyst Characterisation

Powder X-Ray diffraction (PXRD) was performed on a Bruker D8 diffractometer with Co fine focus X-ray source (Ni filter, $\lambda_{K\alpha} = 1.79021$ Å, Θ - Θ geometry, VDS, Lynxeye detector) for samples of the normal synthesis route and on a STOE-Stadi P with Cu fine focus X-ray source (monochromator, $\lambda_{K\alpha 1} = 1.54056$ Å, Θ - Θ geometry, MYTHEN2 R1K detector) for samples of the reverse strike synthesis route. The selected intensity data were collected in the 2θ range from 20 to 85°. Qualitative phase identification was achieved by diffraction pattern assignment according to ICDD data (International Centre for Diffraction Data). Following ICDD data are used: CeO₂ ICDD#75-76, α -Bi₂O₃ ICDD#71-2274, and β -Bi₂O₃ ICDD#78-1793. Crystalline phases were identified through Rietveld refinement with the program TOPAS version 4.2 according to [19–21] adapted for the cerium-bismuth mixed oxides. Instrumental parameters for the fundamental parameter TOPAS refinement were determined by refinement of a LaB₆ reference sample diffraction pattern.

Raman spectra were recorded with an inVia Raman Microscope from Renishaw Corp. A frequency-doubled Nd:Yag laser of the model RL473C from Renishaw with a wavelength of $\lambda = 532$ nm and a UVDD-CCD-Array detector with a grid consisting of 1800 lines/mm was used. The laser power depends on the measuring time. Usually laser powers of 0.5% of the maximal laser power $P = 50$ mW and a measuring time of $t = 60$ s were employed. The calcined samples were placed on a 96-well microplate with V-shaped bottom from Greiner Corp. The microscope was used in line focus. The sample were measured at three different points.

The determination of the specific surface according to Brunauer, Emmett and Teller was performed on a NOVA touch LX4 surface area and pore size analyzer from Quantachrome Corp. The evaluation was performed with the program TouchWinTM version 1.11 from Quantachrome Corp. The specific surface was measured by N₂ adsorption-desorption isotherms at the temperature of liquid N₂ ($T = -196$ °C). The samples were degassed under high vacuum for $t = 4$ h at $T = 250$ °C prior to the measurement. To determine the specific surface S_{BET} , the seven-point BET multi-point method in a relative pressure range of 0.02–0.25 was used.

Energy-dispersive X-ray fluorescence (XRF) analyses to determine the mass fractions of Bi and Ce were performed on a FISCHERSCOPE®X-RAY XAN®instrument and the evaluations were conducted with the program WinFTM®from Fischer Corp. The excitation voltage was $U = 30$ keV and the measuring time $t = 60$ s. The catalysts which were calcined at $T = 800$ °C were placed on top of a cellulose foil. Three repeated measurements at different points of the sample were employed and averaged in composition. Calibration of the measurement data was done by a standardless fundamental parameter method supplied by Fischer Corp (for more details see [22–25]).

3. Results

3.1. Raman and PXRD Analysis

As depicted in the Raman spectra in Figure 1, the synthesized $\text{Ce}_{1.0}\text{Bi}_{0.0}\text{O}_x$ (pure ceria) samples for both co-precipitation routes show one band at $\nu = 462 \text{ cm}^{-1}$. Note that with “x” we denote in the following that the amount of oxygen is variable and depending on preparation conditions, whereas the other subscripts in the all formulae represent the molar composition. The band at $\nu = 462 \text{ cm}^{-1}$ was attributed to the F_{2g} mode of CeO_2 [26]. This confirms that the pure CeO_2 was synthesized in both cases without any defect structure. For the $\text{Ce}_{0.0}\text{Bi}_{1.0}\text{O}_x$ (pure bismuth(III) oxide) all bands typical for $\alpha\text{-Bi}_2\text{O}_3$ were observed for both synthesis methods. These bands were the following one: $\nu = 120 \text{ cm}^{-1}$, 140 cm^{-1} , 152 cm^{-1} , 184 cm^{-1} , 212 cm^{-1} , 281 cm^{-1} , 314 cm^{-1} , 411 cm^{-1} , 449 cm^{-1} , and 532 cm^{-1} [26–29]. For both synthesis routes, with increasing Ce content the F_{2g} band of CeO_2 dominates the Raman spectra but with a higher F_{2g} band FWHM (full width at half maximum, see supplementary information Table S1) compared to the intense F_{2g} band of the $\text{Ce}_{1.0}\text{Bi}_{0.0}\text{O}_x$ spectra.

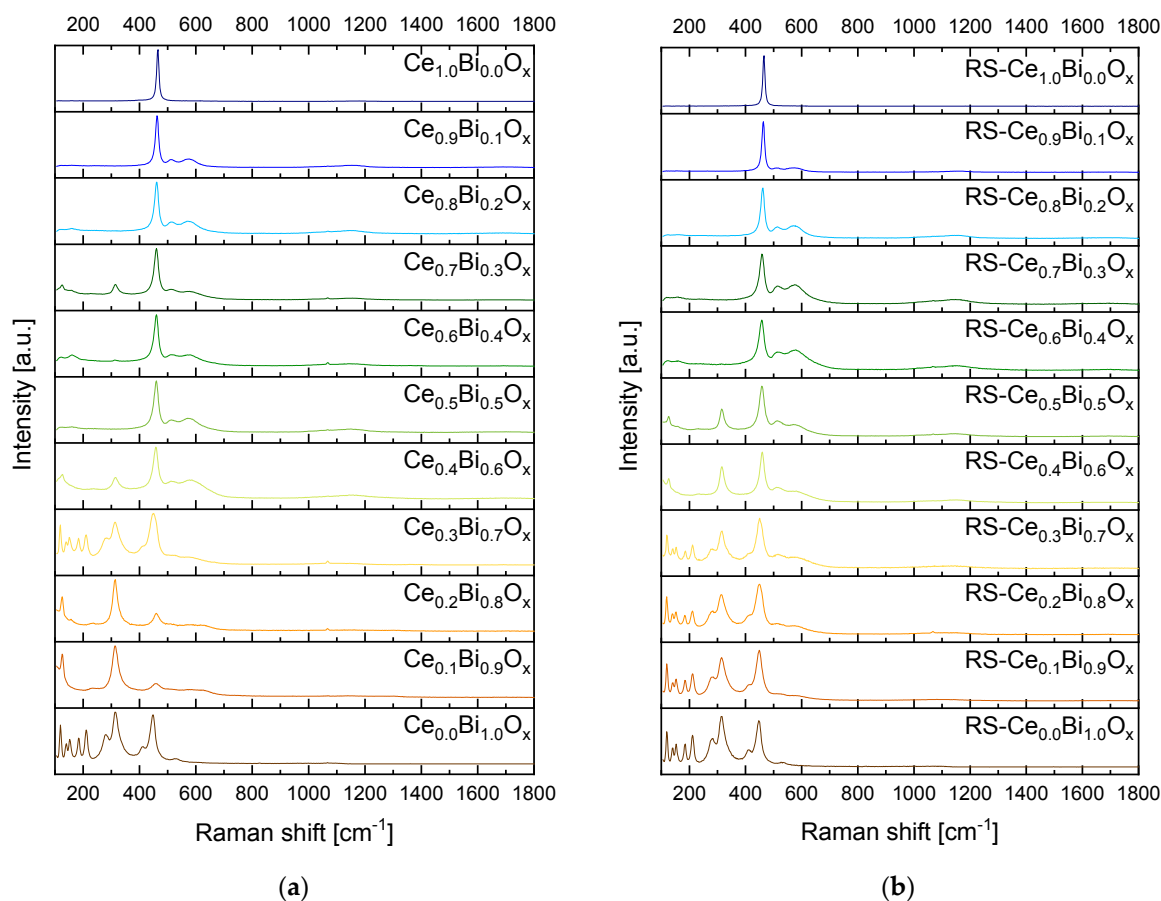


Figure 1. Raman spectra of the synthesized Bi-Ce-mixed oxides with varying Bi-Ce-molar ratios in 10 mol% steps. Each sample is measured three times. Shown are representative spectra of these measurements. All spectra are normalized for comparison. Oxides have been calcined at $T = 800 \text{ }^\circ\text{C}$. Laser wavelength is $\lambda = 532 \text{ nm}$. (a) Normal synthesis route; (b) Reverse strike synthesis route.

Figure 1a shows the Raman spectra of the normal co-precipitation route. In the range from $\text{Ce}_{0.1}\text{Bi}_{0.9}\text{O}_x$ to $\text{Ce}_{0.4}\text{Bi}_{0.6}\text{O}_x$ bands for $\beta\text{-}$ and $\alpha\text{-Bi}_2\text{O}_3$ can be identified. Especially, the spectra of the compositions $\text{Ce}_{0.1}\text{Bi}_{0.9}\text{O}_x$, $\text{Ce}_{0.2}\text{Bi}_{0.8}\text{O}_x$, and $\text{Ce}_{0.4}\text{Bi}_{0.6}\text{O}_x$ show the band profile of $\beta\text{-Bi}_2\text{O}_3$ with the following typical bands: $\nu = 125 \text{ cm}^{-1}$, 232 cm^{-1} , 314 cm^{-1} , and 462 cm^{-1} [29]. Through position-resolved Raman micro-spectroscopy at different locations of the samples, we found that the

samples were inhomogeneous with regards to phase composition. Areas with predominantly α -Bi₂O₃ and areas with β -Bi₂O₃ mixed with CeO₂ were observed. The F_{2g} band of CeO₂ at $\nu = 464 \text{ cm}^{-1}$ and the band of β -Bi₂O₃ at $\nu = 466 \text{ cm}^{-1}$ are overlapping [26,29]. Therefore, it is hardly possible to distinguish between CeO₂ and β -Bi₂O₃ in the range of high Bi content. With increasing Ce content, the typical bands for the bismuth oxides are disappearing and the F_{2g} band of CeO₂ dominates the spectra except the spectrum for Ce_{0.7}Bi_{0.3}O_x. This spectrum contains bands for β -Bi₂O₃ and CeO₂. The spectra for Ce_{0.8}Bi_{0.2}O_x and Ce_{0.9}Bi_{0.1}O_x show two broad bands at $\nu = 510 \text{ cm}^{-1}$ and 570 cm^{-1} . According to Schilling et al. these bands can be assigned to oxygen vacancy formation $\text{Ce}^{3+}\text{O}_7\text{Vo}$ and $\text{Ce}^{4+}\text{O}_7\text{Vo}$ [26]. Figure 1b shows the Raman spectra of the reverse strike co-precipitation samples. The oxides RS-Ce_{0.1}Bi_{0.9}O_x, RS-Ce_{0.2}Bi_{0.8}O_x, and RS-Ce_{0.3}Bi_{0.7}O_x show clearly the typical bands originating from α -Bi₂O₃. The two oxides RS-Ce_{0.4}Bi_{0.6}O_x and RS-Ce_{0.5}Bi_{0.5}O_x have the typical F_{2g} band of CeO₂ and the bands of β -Bi₂O₃. From RS-Ce_{0.6}Bi_{0.4}O_x to RS-Ce_{0.9}Bi_{0.1}O_x only the F_{2g} band and the two bands at $\nu = 510 \text{ cm}^{-1}$ and 570 cm^{-1} resulting from the defects of the fluorite-type structure are to be recognized.

Figure 2 presents the PXRD pattern of the synthesized samples for both synthesis routes. In general, the PXRD data confirm the results from Raman analyses. For both synthesis routes, the PXRD pattern shows that the oxides Ce_{0.0}Bi_{1.0}O_x adopt the monoclinic α -Bi₂O₃ crystal structure with space group P2₁/c. The synthesized Ce_{1.0}Bi_{0.0}O_x crystallises cubic in a fluorite-type structure with the space group Fm $\bar{3}$ m. The PXRD pattern of the mixed oxides with increasing Bi content shows that, additionally to the reflections of ceria lattice structure, diffraction signals of the monoclinic α -Bi₂O₃ structure and of the tetragonal β -Bi₂O₃ with space group P4₂1c are appearing. For the normal synthesis route, only for the oxides Ce_{0.8}Bi_{0.2}O_x and Ce_{0.9}Bi_{0.1}O_x a single phase of Bi³⁺-doped CeO₂ was observed. The lattice parameter *a* and the mass fraction of Bi³⁺ in the CeO₂ lattice have been determined by Rietveld refinement. Doping CeO₂ with Bi³⁺ increases the lattice parameter *a* from 5.4110(1) Å for CeO₂ to 5.4174(1) Å for Ce_{0.9}Bi_{0.1}O_x and further on 5.4235(1) Å for Ce_{0.8}Bi_{0.2}O_x. In contrast, with the reverse strike synthesis route in the range of pure ceria to RS-Ce_{0.6}Bi_{0.4}O_x a single Bi³⁺-doped CeO₂ crystalline phase was observed, and the range of existence was thus broader than for the normal precipitation process. Figure 3 shows the lattice parameter *a* from Rietveld refinement of the Bi³⁺-doped CeO₂ phases, and in Tables S2 and S3 all refined parameters are specified in detail. The insertion of Bi³⁺ ions into the CeO₂ lattice increased the lattice parameter. For RS-Ce_{0.6}Bi_{0.4}O_x the lattice parameter *a* was 5.4273(3) Å. The lattice parameter *a* for the synthesized pure RS-CeO₂ was 5.4071(1) Å.

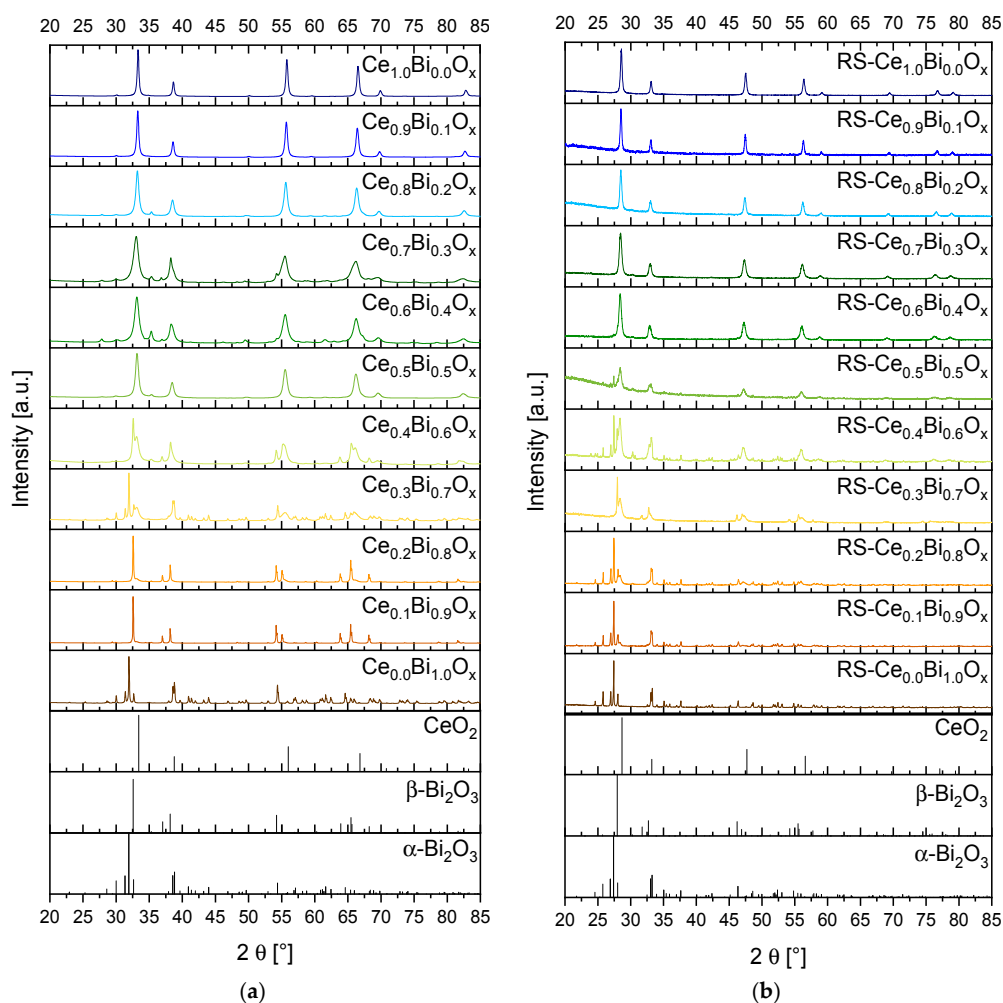


Figure 2. Powder X-ray diffraction (PXRD) pattern of the synthesized Bi-Ce mixed oxides with varying Bi-Ce molar ratios in 10 mol% steps. Oxides calcined at $T = 800$ °C. (a) Normal synthesis route. Measured with $\text{Co-K}\alpha$ radiation, $\lambda = 178.92$ nm; (b) Reverse strike synthesis route. Measured with $\text{Cu-K}\alpha$ radiation, $\lambda = 154.06$ nm. Reference files for CeO_2 : ICDD#75-76; $\alpha\text{-Bi}_2\text{O}_3$: ICDD#71-2274; $\beta\text{-Bi}_2\text{O}_3$: ICDD#78-1793.

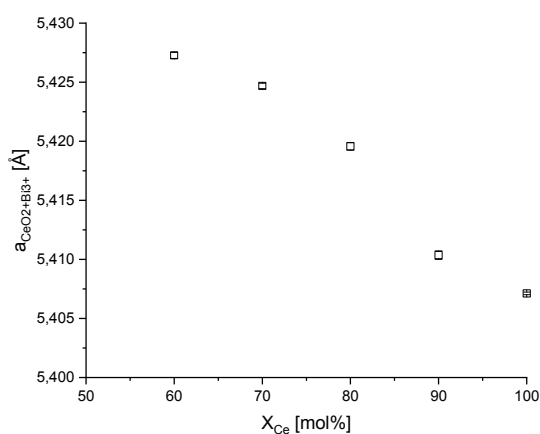


Figure 3. Lattice parameter a with standard deviation (STD) of a of cubic fluorite-type Bi^{3+} -doped CeO_2 phase in dependence of the nominal molar Ce content determined by Rietveld refinement with the program TOPAS [30].

3.2. XRF and BET Results

To verify the nominal Bi and Ce metal mass percentages of the oxides, i.e. without inclusion of oxygen content, XRF measurements were performed. Table 2 shows the acquired mass percentages. Note that there were no larger deviations between nominal and the expected mass percentages of the samples. Furthermore, the mass percentages of Bi and Ce differed not more than 2% between the two synthesis routes.

Table 2. Mass percentages m% of the synthesized mixed oxides determined by X-ray fluorescence (XRF) analysis. Shown are the averaged values of three repeated measurements of one sample at different areas with standard deviations.

Composition of Oxide Formulae	Nominal Mass Percentages		Measured Mass Percentage			
	m%Ce	m%Bi	Normal Synthesis		Reverse Strike Synthesis	
	m%Ce	m%Bi	m%Ce	m%Bi	m%Ce	m%Bi
Ce _{0.0} Bi _{1.0} O _x	0.00	100.00	0.00 ± 0.00	100.0 ± 0.00	0.00 ± 0.00	100.0 ± 0.00
Ce _{0.1} Bi _{0.9} O _x	7.59	92.41	6.89 ± 0.17	92.85 ± 0.15	7.52 ± 0.15	92.48 ± 0.15
Ce _{0.2} Bi _{0.8} O _x	15.59	84.41	14.36 ± 0.16	85.26 ± 0.16	15.15 ± 0.44	84.85 ± 0.44
Ce _{0.3} Bi _{0.7} O _x	24.05	75.95	22.86 ± 0.26	76.51 ± 0.30	23.52 ± 0.04	76.48 ± 0.04
Ce _{0.4} Bi _{0.6} O _x	33.00	67.00	31.71 ± 0.21	67.64 ± 0.26	30.07 ± 0.55	69.31 ± 0.45
Ce _{0.5} Bi _{0.5} O _x	42.49	57.51	45.52 ± 1.33	54.18 ± 1.64	44.09 ± 0.19	55.91 ± 0.19
Ce _{0.6} Bi _{0.4} O _x	52.56	47.44	57.13 ± 0.44	42.27 ± 0.19	55.58 ± 0.20	44.42 ± 0.20
Ce _{0.7} Bi _{0.3} O _x	63.29	36.71	60.64 ± 0.74	38.50 ± 0.79	58.25 ± 0.37	40.71 ± 0.36
Ce _{0.8} Bi _{0.2} O _x	74.72	25.28	75.42 ± 0.75	23.85 ± 0.27	78.66 ± 0.10	21.34 ± 0.10
Ce _{0.9} Bi _{0.1} O _x	86.93	13.07	85.64 ± 0.40	13.96 ± 0.16	89.17 ± 0.09	10.83 ± 0.09
Ce _{1.0} Bi _{0.0} O _x	100.00	0.00	100.0 ± 0.00	0.00 ± 0.00	100.0 ± 0.00	0.00 ± 0.00

Table 3 shows the total surface area S_{BET} of the synthesized samples determined by N₂ physisorption experiments. The S_{BET} was determined by the multi-point BET method. For the normal precipitation route, the pure Bi₂O₃ had with $S_{BET} = 0.4 \text{ m}^2 \cdot \text{g}^{-1}$ the lowest specific surface. With increasing Ce content, the S_{BET} increases as well. The highest surface area was observed for the pure CeO₂ with $S_{BET} = 26.6 \text{ m}^2 \cdot \text{g}^{-1}$. For the compositions Ce_{0.6}Bi_{0.4}O_x with $S_{BET} = 18.7 \text{ m}^2 \cdot \text{g}^{-1}$ and Ce_{0.8}Bi_{0.2}O_x with $S_{BET} = 13.1 \text{ m}^2 \cdot \text{g}^{-1}$ also relatively high surface areas within this test series were observed. Surprisingly, the composition Ce_{0.7}Bi_{0.3}O_x has only a S_{BET} of $6.5 \text{ m}^2 \cdot \text{g}^{-1}$. The differences in the observed Raman and PXRD data of this composition compared to others also reflected this behavior.

Table 3. Calculated specific surface areas according to Brunauer, Emmett, and Teller (S_{BET}) of the synthesized mixed Bi-Ce oxides determined by nitrogen adsorption measurements. Oxides are calcined at $T = 800 \text{ }^\circ\text{C}$.

Composition of Oxide	$S_{BET,normal \text{ synthesis}} [\text{m}^2 \cdot \text{g}^{-1}]$	$S_{BET,reverse \text{ strike synthesis}} [\text{m}^2 \cdot \text{g}^{-1}]$
Ce _{0.0} Bi _{1.0} O _x	0.4	2.0
Ce _{0.1} Bi _{0.9} O _x	1.5	1.0
Ce _{0.2} Bi _{0.8} O _x	2.2	2.1
Ce _{0.3} Bi _{0.7} O _x	5.4	1.0
Ce _{0.4} Bi _{0.6} O _x	6.4	1.5
Ce _{0.5} Bi _{0.5} O _x	7.8	2.2
Ce _{0.6} Bi _{0.4} O _x	18.7	6.7
Ce _{0.7} Bi _{0.3} O _x	6.5	15.1
Ce _{0.8} Bi _{0.2} O _x	13.1	21.3
Ce _{0.9} Bi _{0.1} O _x	20.2	11.6
Ce _{1.0} Bi _{0.0} O _x	26.6	6.2

For the reverse strike co-precipitation route, as Ce content increased the S_{BET} also increased. The maximum of the surface area was reached at a Ce content of 80 mol% with $S_{BET} = 21.3 \text{ m}^2 \cdot \text{g}^{-1}$. A further

increase of the Ce content led to a decrease in S_{BET} . For pure CeO_2 prepared by the reverse-strike precipitation method only $S_{BET} = 6.2 \text{ m}^2 \cdot \text{g}^{-1}$ was observed.

3.3. OSC_{dyn} and TGA Results

The dynamic oxygen storage capacities OSC_{dyn} were measured via thermogravimetric analyses in defined gas atmospheres and are shown in Table 4. First, each sample was heated with a specific heating rate under nitrogen for desorption of compounds like water, and to reduce the sample to substoichiometric oxides. Second, the sample was cooled under synthetic air. At this period, the sample was reoxidized. These two steps were repeated. The second reoxidation step was used for calculating the OSC_{dyn} as difference in masses under the two atmospheres at specific temperatures (see chapter 2.2. for details). The OSC_{dyn} is an important factor for the Diesel soot oxidation because the total available surface lattice oxygen is related to the OSC [31]. For the normal synthesis route, $Ce_{0.8}Bi_{0.2}O_x$ had the highest OSC_{dyn} with $34.0 \mu\text{mol}_{O_2} \cdot \text{g}_{\text{cat}}^{-1}$ and $Ce_{0.0}Bi_{1.0}O_x$ revealed the lowest OSC_{dyn} with $1.6 \mu\text{mol}_{O_2} \cdot \text{g}_{\text{cat}}^{-1}$. For this synthesis route, there was no obvious correlation between the composition of oxide and the determined OSC_{dyn} . In contrast to that, the OSC_{dyn} for the reverse strike synthesis route was lower. Nevertheless, a correlation between the composition of oxide and the determined OSC_{dyn} seems to exist. Starting from pure bismuth oxide the OSC_{dyn} increased with an increase in Ce content. The composition RS- $Ce_{0.8}Bi_{0.2}O_x$ with a value of $OSC_{dyn} = 26.4 \mu\text{mol}_{O_2} \cdot \text{g}_{\text{cat}}^{-1}$ seems to represent the maximum in this synthesis series. After that, the OSC_{dyn} decreased to a value of $1.9 \mu\text{mol}_{O_2} \cdot \text{g}_{\text{cat}}^{-1}$ for RS- $Ce_{1.0}Bi_{0.0}O_x$. Furthermore, it is to be noted that the OSC_{dyn} in the intermediate range between the pure cerium oxides and bismuth oxides were different for both synthesis routes. The OSC_{dyn} for the reverse strike co-precipitation of pure bismuth oxide was eight times higher than for the normal synthesis route and the reverse strike co-precipitation of pure cerium oxide was 13 times smaller than the normal synthesis route. The S_{BET} reflected the same trend. There, the S_{BET} for the reverse strike route was five times higher than the normal synthesis route. This shows clearly that the OSC_{dyn} really represents a surface parameter, in this case the surface oxygen lattice ions to be utilized for oxidation processes.

Table 4. Calculated dynamic oxygen storage capacity (OSC_{dyn}) of the synthesized mixed oxides determined by thermogravimetric analysis (TGA). Measurement temperature in the range of $T = 150\text{--}700 \text{ }^\circ\text{C}$ with heating rate of $r = 5 \text{ }^\circ\text{C} \cdot \text{min}^{-1}$ in synthetic air and nitrogen. The average of double determination with the standard deviation is shown.

Composition of Oxide	$OSC_{dyn,normal \text{ synthesis}}$ [$\mu\text{mol}_{O_2} \cdot \text{g}_{\text{cat}}^{-1}$]	$OSC_{dyn,reverse \text{ strike synthesis}}$ [$\mu\text{mol}_{O_2} \cdot \text{g}_{\text{cat}}^{-1}$]
$Ce_{0.0}Bi_{1.0}O_x$	1.6 ± 1.5	13.4 ± 1.0
$Ce_{0.1}Bi_{0.9}O_x$	12.6 ± 7.9	1.9 ± 0.0
$Ce_{0.2}Bi_{0.8}O_x$	10.7 ± 0.9	1.4 ± 0.0
$Ce_{0.3}Bi_{0.7}O_x$	11.3 ± 0.3	2.9 ± 2.4
$Ce_{0.4}Bi_{0.6}O_x$	13.9 ± 1.5	5.4 ± 1.1
$Ce_{0.5}Bi_{0.5}O_x$	24.7 ± 4.6	9.6 ± 0.2
$Ce_{0.6}Bi_{0.4}O_x$	20.3 ± 1.8	18.5 ± 0.9
$Ce_{0.7}Bi_{0.3}O_x$	13.3 ± 3.5	26.0 ± 1.6
$Ce_{0.8}Bi_{0.2}O_x$	34.0 ± 0.4	26.4 ± 5.0
$Ce_{0.9}Bi_{0.1}O_x$	23.4 ± 5.7	17.3 ± 2.3
$Ce_{1.0}Bi_{0.0}O_x$	24.7 ± 2.0	1.9 ± 0.7

In thermogravimetric (TGA) measurement data, the T_{50} value is used to characterise the activity for the Diesel soot oxidation. The T_{50} value describes the temperature where 50% of the model soot is oxidized in a model gas mixture of defined flow rate and heating rate. This value is commonly used in the literature. Table 5 presents the determined T_{50} values. Only the T_{50} values of tight soot-catalyst contact conditions were presented, but also other contact modes were prepared and screened.

Table 5. T_{50} values for Diesel soot oxidation in tight contact mode of the synthesized mixed oxides determined by TGA. Measurement temperature in the range of $T = 25\text{--}700$ °C with heating rate of $r = 5$ °C·min⁻¹ in synthetic air. The averages of double determination with standard deviations are given.

Composition of Oxide	$T_{50,\text{normal synthesis}}$ [°C]	$T_{50,\text{reverse strike synthesis}}$ [°C]
Ce _{0.0} Bi _{1.0} O _x	537.7 ± 0.5	549.1 ± 1.1
Ce _{0.1} Bi _{0.9} O _x	518.4 ± 2.1	549.1 ± 1.8
Ce _{0.2} Bi _{0.8} O _x	507.6 ± 1.4	554.8 ± 1.3
Ce _{0.3} Bi _{0.7} O _x	483.9 ± 0.5	558.0 ± 1.0
Ce _{0.4} Bi _{0.6} O _x	519.8 ± 1.4	555.4 ± 2.3
Ce _{0.5} Bi _{0.5} O _x	494.0 ± 0.5	543.9 ± 1.0
Ce _{0.6} Bi _{0.4} O _x	480.2 ± 0.2	534.9 ± 2.0
Ce _{0.7} Bi _{0.3} O _x	489.3 ± 1.5	498.7 ± 0.2
Ce _{0.8} Bi _{0.2} O _x	450.3 ± 0.8	443.7 ± 2.7
Ce _{0.9} Bi _{0.1} O _x	457.5 ± 0.1	525.9 ± 0.8
Ce _{1.0} Bi _{0.0} O _x	509.2 ± 1.6	585.8 ± 1.7

The lowest T_{50} value was reached for the compositions Ce_{0.8}Bi_{0.2}O_x and RS-Ce_{0.8}Bi_{0.2}O_x. Like for the S_{BET} and OSC_{dyn} , there was a less distinct correlation between T_{50} and the composition of the oxide for the normal synthesis route indicating nuisance factors in the syntheses. In contrast to the normal synthesis route, there was a clear dependency in T_{50} values as a function of oxide composition for the reverse strike synthesis route. Starting from pure bismuth oxide the T_{50} decreased with higher Ce content to a minimum for composition RS-Ce_{0.8}Bi_{0.2}O_x with a T_{50} value of 444 °C. After that, the T_{50} value increased again to 586 °C for RS-Ce_{1.0}Bi_{0.0}O_x. In general, and for both synthesis routes, the T_{50} values of pure CeO₂ and Bi₂O₃ were higher than that of the mixed oxides.

4. Discussion

4.1. Normal Synthesis Route

PXRD data refinements reveal that in compositions with high Bi content two crystalline Bi₂O₃ phases can be detected, i.e., monoclinic α -Bi₂O₃ and tetragonal β -Bi₂O₃. Additionally reflections representing about 5m% bismutite Bi₂(CO₃)O₂ can also be detected in PXRD determined by Rietveld refinement. Confirmation of these results is achieved by Raman spectroscopy. With increasing Ce content up to the composition Ce_{0.7}Bi_{0.3}O_x, a β -Bi₂O₃ phase is present. One reason for this observation could be the initial stages of precipitation of the oxides. From a visual inspection of the precipitation process, we find the beginning of precipitation for bismuth oxide at $\text{pH} < 1$ and for cerium oxide near to $\text{pH} = 4$. After calcination, the α -Bi₂O₃ polymorph should be formed as this is the thermodynamic stable form [32]. Additionally, it is known that hydrated bismuth oxides oligomerise in aqueous acidic media [18]. In our case, also the β -Bi₂O₃ form is present. The oligomerisation of the hydrated bismuth oxides at low pH values and the incorporation of cerium oxide into the crystal lattice, may both serve as an explanation for the observation of the tetragonal β -Bi₂O₃ form. Another reason is that the formation of β -Bi₂O₃ may result from decomposition of bismutite [33]. With increasing Ce content, the F_{2g} mode in the Raman spectra gets the dominant band. Above a Ce content of 50 mol% there are two more bands to be assigned to CeO₂. The band at $\nu \sim 510$ cm⁻¹ is caused by the formation of Ce³⁺ ions in combination with oxygen vacancies. The band at $\nu \sim 570$ cm⁻¹ originates from oxygen vacancies in combination with Ce⁴⁺ ions (see above and ref. [19]). From Figure 1 it can be seen that these two defect bands are most noticeable for the compositions Ce_{0.8}Bi_{0.2}O_x and Ce_{0.9}Bi_{0.1}O_x and that in the samples with these compositions only the Bi³⁺-doped CeO₂ phase is verifiable. Interestingly, these two compositions have, for this synthesis route, the lowest T_{50} values and highest OSC_{dyn} values compared to the other compositions. This is illustrated in Figure 4.

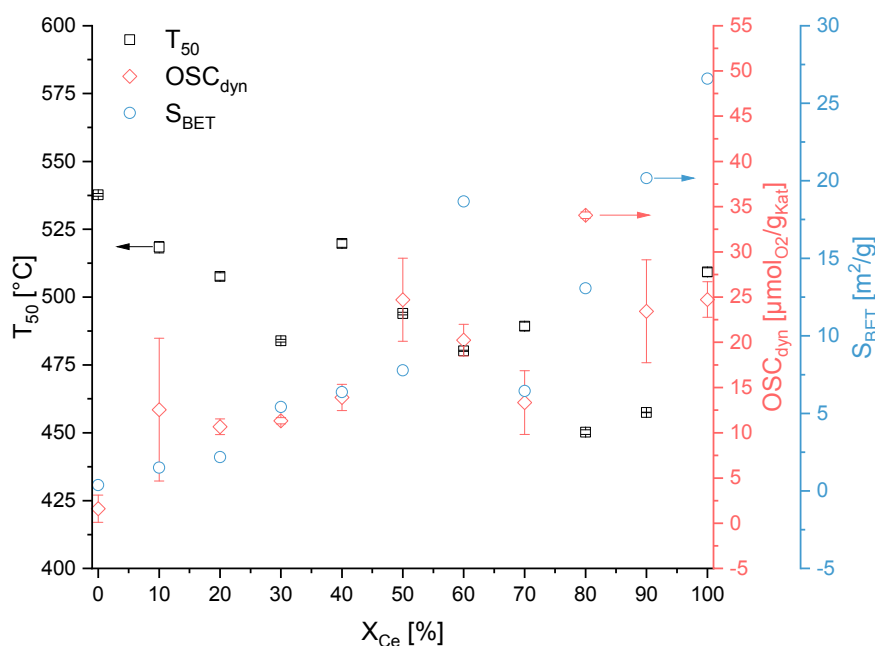


Figure 4. T_{50} (tight contact), S_{BET} and OSC_{dyn} values in dependence of the nominal molar Ce content for samples prepared by normal precipitation. Shown are duplicate measurements together with their standard deviation.

4.2. Reverse Strike Synthesis Route

To avoid the oligomerisation of the hydrated bismuth oxides in aqueous acidic media and the sequential precipitation of oxides with different compositions, i.e., cerium and bismuth oxides separately, the reverse strike co-precipitation method is applied. During this synthesis route, the premixed acidic precursor solutions are added to the basic precipitation agent solution. The precipitation is stopped at $\text{pH} = 6$. Therefore, an acidic pH range is avoided. According to the PXRD data, see Figure 2b, below a molar fraction of 60 mol% Ce only a Bi^{3+} -doped CeO_2 phase is observed. These results are in accordance to the results of Hund *et al.* [15]. Compared to the normal synthesis route, with the reverse strike route the mixed oxide phase extends to even lower Ce fractional amounts. These results are supported by Raman analyses (see Figure 1b). Additionally, only bismutite is present in the Raman spectra of $\text{Ce}_{0.2}\text{Bi}_{0.8}\text{O}_x$ to $\text{Ce}_{0.8}\text{Bi}_{0.2}\text{O}_x$ as an additional phase in a minor amount. Furthermore, the two defect bands at $\nu = 510 \text{ cm}^{-1}$ and $\nu = 570 \text{ cm}^{-1}$ are very prominent within the composition range of $\text{Ce}_{0.6}\text{Bi}_{0.4}\text{O}_x$ to $\text{Ce}_{0.8}\text{Bi}_{0.2}\text{O}_x$. At higher Ce content the intensity of the two defect bands decreases again, and are not to be detected in the Raman spectrum of $\text{Ce}_{1.0}\text{Bi}_{0.0}\text{O}_x$. In Section 3.1. we concluded that the formation of oxygen sublattice defects in ceria of fluorite-structure type may influence the activity of the catalyst for the Diesel soot oxidation. The more pronounced the defect structure is, the higher the activity will be for Diesel soot oxidation. In Figure 5, the correlation between T_{50} , OSC_{dyn} and S_{BET} is presented for the samples of this synthesis route. For this synthesis series, a clear correlation between activity and characterization data can be seen. Starting from pure ceria with increasing Bi content, T_{50} values decrease revealing that the soot oxidation activity increases. At the same time, both OSC_{dyn} and S_{BET} increase. This trend reaches its maximum – low T_{50} value and high OSC_{dyn} and S_{BET} – at 80 mol% Ce content. This is in accordance with the described effect of the Raman spectra with the two defect bands at $\nu = 510 \text{ cm}^{-1}$ and $\nu = 570 \text{ cm}^{-1}$. At still lower Ce content, the T_{50} values increase, and the OSC_{dyn} and S_{BET} values decrease again. In the same sequence, the intensities of the two defect bands in Raman spectra decrease. The two defect bands are not detected in the Raman spectrum of pure ceria.

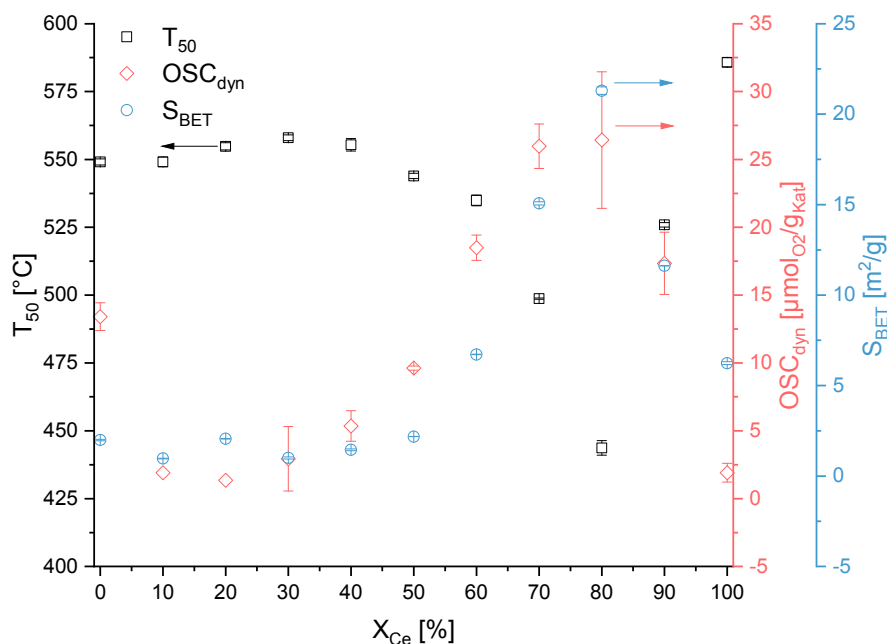
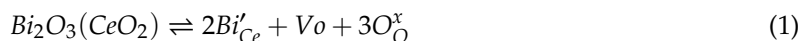


Figure 5. T_{50} (tight contact), S_{BET} and OSC_{dyn} values in dependence of the nominal molar Ce content for samples prepared by reverse strike precipitation. Shown are duplicate measurements with their standard deviation.

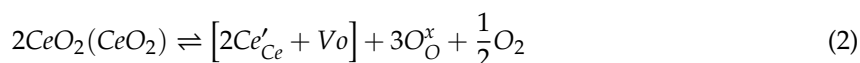
5. Conclusions

In this paper, two automated routes of co-precipitation methods to synthesize a complete series of Bi-Ce mixed oxides $Ce_{1-x}Bi_xO_{2-x/2}$ ($0 \leq x \leq 1$) for catalytic oxidation of Diesel soot are described: The normal synthesis and the reverse strike synthesis. The synthesized oxides are characterized by PXRD, Raman spectroscopy, and nitrogen adsorption to measure the specific surface. Furthermore, the dynamic oxygen storage capacities OSC_{dyn} are determined by TGA methods. The catalytic activities are also measured by TGA under continuous gas flow conditions and specified by T_{50} values. Raman spectroscopy reveals that, with an increasing Ce content, an oxygen defect structure of the fluorite-type ceria lattice as a result of Bi^{3+} insertion into the cation sublattice occurs (in Kröger-Vink notation, see equation 1):



At least two bands resulting from oxygen defects of the ceria lattice are observed in the Raman spectra. Additionally, a relation between OSC_{dyn} , S_{BET} and T_{50} values is found indicating that catalytic activity for Diesel soot oxidation and defect structure are highly correlated. This relation is very striking for the mixed oxides, which are synthesized through the reverse strike method, but less distinct for samples prepared by the normal precipitation route. Here, the maximal catalytic activity with the maximal OSC_{dyn} and S_{BET} is reached at the maximal intensity of the two defect bands in the Raman spectra at the optimal composition of $Ce_{0.8}Bi_{0.2}O_{1.9}$. Compared to the pure reverse strike co-precipitated CeO_2 RS- $Ce_{1.0}Bi_{0.0}O_x$, the T_{50} decreases from 586 °C to 444 °C. This is an improvement of $\Delta T_{50} \approx 140$ °C. Simultaneously, the OSC_{dyn} increases from 1.9 $\mu\text{mol}_{O_2} \cdot \text{g}_{\text{cat}}^{-1}$ for the RS- $Ce_{1.0}Bi_{0.0}O_x$ to 26.4 $\mu\text{mol}_{O_2} \cdot \text{g}_{\text{cat}}^{-1}$ for the RS- $Ce_{0.8}Bi_{0.2}O_x$. This is an increase of $\Delta OSC_{dyn} = 24.5 \mu\text{mol}_{O_2} \cdot \text{g}_{\text{cat}}^{-1}$. Additionally, the S_{BET} also increases from 6.2 $\text{m}^2 \cdot \text{g}^{-1}$ for the RS- $Ce_{1.0}Bi_{0.0}O_x$ to 21.3 $\text{m}^2 \cdot \text{g}^{-1}$ for the RS- $Ce_{0.8}Bi_{0.2}O_x$. This is an increase of $\Delta S_{BET} = 15.1 \text{m}^2 \cdot \text{g}^{-1}$. PXRD data reveal that with this composition we are still in the phase field of a cubic defect structure of the fluorite-type structure and that the field of stability for this mixed oxide phase is limited to the compositional range $0 \leq x \leq 0.4$. At higher x also pure bismuth oxide phases are formed. Due to ionic radii differences ($r(Bi^{3+}) = 1.03 \text{ \AA}$, $r(Ce^{3+}) = 1.01 \text{ \AA}$, $r(Ce^{4+}) = 0.87 \text{ \AA}$, all for CN = 6 [34]) the incorporation of Bi^{3+} into the ceria

lattice $\text{Ce}^{4+}(\text{O}^{2-})_2$ “widens” the crystal lattice as can be seen from the increase in the lattice parameter a . Additionally, due to the lone pair configuration of Bi^{3+} , a local distortion of the cation coordination environment by oxygen anions occurs. Both factors facilitate the incorporation of larger Ce^{3+} ions into the cationic Ce^{4+} sublattice, thus, increasing the oxygen storage capacity, as for each O^{2-} removed for charge neutrality two Ce^{4+} ions have to be reduced to Ce^{3+} (so-called Schottky defect set in square brackets, see equation 2):



As on the other side, too much Bi^{3+} is destabilising the lattice, as seen from the crystallisation of additional bismuth oxide phases. There is an optimum of oxygen storage capacity and thus minimum of T_{50} value, in this case at $x = 0.2$.

Supplementary Materials: The following are available online at <http://www.mdpi.com/1996-1944/13/6/1369/s1>. Table S1: FWHM (full width at half maximum) of the F_{2g} band from the CeO_2 lattice of Raman spectra. Given is the average of three repeated measurements and the standard deviation. FWHM is determined with the software Origin Pro 2019b; Table S2: Results of Rietveld-Refinement of the normal precipitation route. Samples are calcined by $T = 800$ °C; Table S3: Results of Rietveld-Refinement of the reverse strike precipitation route. Samples are calcined by $T = 800$ °C.

Author Contributions: S.C.H. build the experimental setups, conducted experiments, analyzed data and wrote this paper. K.S. supervised the work and reviewed the article. All authors have read and agreed to the published version of the manuscript.

Funding: This research received no external funding.

Acknowledgments: We thank the professorship Coordination Chemistry (Prof. M. Mehring, M.Sc. I. Köwitsch) at TUC for measuring PXRD pattern and the professorship of Material and Surface Engineering (Prof. T. Lampke, M.Sc. Th. Mehner, M.Sc. Pügner, Dipl.-Ing. E. Benedix) at TUC for the possibility to measure XRF as well as measuring PXRD pattern.

Conflicts of Interest: The authors declare no conflict of interest.

References

- Janssen, N.A.; Gerlofs-Nijland, M.E.; Lanki, T.; Salonen, R.O.; Cassee, F.; Hoek, G.; Fischer, P.; Brunekreef, B.; Krzyzanowski, M. *Health Effects of Black Carbon*; World Health Organization: Geneva, Switzerland, 2012; pp. 1–86.
- Prasad, R.; Bella, V.R. A review on diesel soot emission, its effect and control. *Bull. Chem. React. Eng. Catal.* **2010**, *5*, 69–86. [[CrossRef](#)]
- Channell, M.M.; Paffett, M.L.; Devlin, R.B.; Madden, M.C.; Campen, M.J. Circulating factors induce coronary endothelial cell activation following exposure to inhaled diesel exhaust and nitrogen dioxide in humans: Evidence from a novel translational in vitro model. *Toxicol. Sci.* **2012**, *127*, 179–186. [[CrossRef](#)] [[PubMed](#)]
- Schwarze, P.E.; Totlandsdal, A.I.; Låg, M.; Refsnes, M.; Holme, J.A.; Øvrevik, J. Inflammation-related effects of diesel engine exhaust particles: Studies on lung cells in vitro. *BioMed Res. Int.* **2013**, *2013*, 685142. [[CrossRef](#)] [[PubMed](#)]
- Johansen, K. Multi-catalytic soot filtration in automotive and marine applications. *Catal. Today* **2015**, *258*, 2–10. [[CrossRef](#)]
- Zhang, Z.H.; Balasubramanian, R. Effects of Cerium Oxide and Ferrocene Nanoparticles Addition As Fuel-Borne Catalysts on Diesel Engine Particulate Emissions: Environmental and Health Implications. *Environ. Sci. Technol.* **2017**, *51*, 4248–4258. [[CrossRef](#)]
- Zhang, B.; Jiaqiang, E.; Gong, J.; Yuan, W.; Zuo, W.; Li, Y.; Fu, J. Multidisciplinary design optimization of the diesel particulate filter in the composite regeneration process. *Appl. Energy* **2016**, *181*, 14–28. [[CrossRef](#)]
- Adler, J. Ceramic diesel particulate filters. *Int. J. Appl. Ceram. Technol.* **2005**, *2*, 429–439. [[CrossRef](#)]
- Krishna, K.; Bueno-López, A.; Makkee, M.; Moulijn, J.A. Potential rare earth modified CeO_2 catalysts for soot oxidation. I. Characterisation and catalytic activity with O_2 . *Appl. Catal. B Environ.* **2007**, *75*, 189–200. [[CrossRef](#)]

10. Sardar, K.; Playford, H.Y.; Darton, R.J.; Barney, E.R.; Hannon, A.C.; Tompsett, D.; Fisher, J.; Kashtiban, R.J.; Sloan, J.; Ramos, S.; et al. Nanocrystalline cerium-bismuth oxides: Synthesis, structural characterization, and redox properties. *Chem. Mater.* **2010**, *22*, 6191–6201. [[CrossRef](#)]
11. Aneggi, E.; Boaro, M.; De Leitenburg, C.; Dolcetti, G.; Trovarelli, A. Insights into the redox properties of ceria-based oxides and their implications in catalysis. *J. Alloys Compd.* **2006**, *408–412*, 1096–1102. [[CrossRef](#)]
12. Wolf, V. Neuartige Katalysatoren für die Oxidation von Dieselruß in der Abgasnachbehandlung von Fahrzeugen. Ph.D. Thesis, Universität des Saarlandes, Saarbrücken, Germany, 2015.
13. Dikmen, S.; Shuk, P.; Greenblatt, M. Hydrothermal synthesis and properties of $Ce_{1-x}Bi_xO_2$ -delta solid solutions. *Solid State Ionics* **1998**, *112*, 299–307. [[CrossRef](#)]
14. Zhao, H.; Feng, S. Hydrothermal Synthesis and Oxygen Ionic Conductivity of Codoped Nanocrystalline $Ce_{1-x}M_xBi_{0.4}O_{2.6-x}$, $M = Ca, Sr, \text{ and } Ba$. *Chem. Mater.* **1999**, *11*, 958–964. [[CrossRef](#)]
15. Hund, F. Fluoritmischphasen der Dioxide von Uran, Thorium, Cer und Zirkonium mit Wismutoxide. *Zeitschrift für Anorg. und Allg. Chemie* **1964**, *333*, 248–255. [[CrossRef](#)]
16. Frolova, Y.V.; Kochubey, D.I.; Kriventsov, V.V.; Moroz, E.M.; Neofitides, S.; Sadykov, V.A.; Zyuzin, D.A. The influence of bismuth addition on the local structure of CeO_2 . *Nucl. Instrum. Methods Phys. Res. Sect. A* **2005**, *543*, 127–130. [[CrossRef](#)]
17. Lee, K.T.; Lidie, A.A.; Jeon, S.Y.; Hitz, G.T.; Song, S.J.; Wachsmann, E.D. Highly functional nano-scale stabilized bismuth oxides via reverse strike co-precipitation for solid oxide fuel cells. *J. Mater. Chem. A* **2013**, *1*, 6199–6207. [[CrossRef](#)]
18. Hollemann, N.W.A.F. *Lehrbuch der Anorganischen Chemie*; 102. Edition; Walter de Gruyter: Berlin, Germany; New York, NY, USA, 2007; pp. 822–860.
19. Cheary, R.W.; Coelho, A.A. A fundamental parameters approach to X-ray line-profile fitting. *J. Appl. Crystallogr.* **1992**, *25*, 109–121. [[CrossRef](#)]
20. Cheary, R.W.; Coelho, A.A.; Cline, J.P. Fundamental parameters line profile fitting in laboratory diffractometers. *J. Res. Natl. Inst. Stand. Technol.* **2004**, *109*, 1–25. [[CrossRef](#)]
21. Kern, A.; Coelho, A.A.; Cheary, R.W. Convolution Based Profile Fitting. In *Diffraction Analysis of the Microstructure of Materials*; Mittemeijer, E.J., Scardi, P., Eds.; Springer: Berlin/Heidelberg, Germany, 2004; pp. 17–50.
22. Lagultton, D.; Parrish, W. Simultaneous Determination of Composition and Mass Thickness of Thin Films by Quantitative X-ray Fluorescence Analysis. *Anal. Chem.* **1977**, *49*, 1152–1156. [[CrossRef](#)]
23. Criss, J.W.; Birks, L.S. Calculation Methods for Fluorescent X-Ray Spectrometry: Empirical Coefficients vs. Fundamental Parameters. *Anal. Chem.* **1968**, *40*, 1080–1086. [[CrossRef](#)]
24. Shiraiwa, T.; Fujino, N. Theoretical Calculation of Fluorescent X-Ray Intensities in Fluorescent X-Ray Spectrochemical Analysis. *Jpn. J. Appl. Phys.* **1966**, *5*, 886–899. [[CrossRef](#)]
25. Ohno, K.; Fujiwara, J.; Morimoto, I. X-ray fluorescence analysis without standards of small particles extracted from super-alloys. *X-Ray Spectrom.* **1980**, *9*, 138–142. [[CrossRef](#)]
26. Schilling, C.; Hofmann, A.; Hess, C.; Ganduglia-Pirovano, M.V. Raman Spectra of Polycrystalline CeO_2 : A Density Functional Theory Study. *J. Phys. Chem. C* **2017**, *121*, 20834–20849. [[CrossRef](#)]
27. Taylor, P.; Sunder, S.; Lopata, V.J. Structure, spectra, and stability of solid bismuth carbonates. *Can. J. Chem.* **1984**, *62*, 2863–2873. [[CrossRef](#)]
28. Selvamani, T.; Anandan, S.; Granone, L.; Bahnemann, D.W.; Ashokkumar, M. Phase-controlled synthesis of bismuth oxide polymorphs for photocatalytic applications. *Mater. Chem. Front.* **2018**, *2*, 1664–1673. [[CrossRef](#)]
29. Salazar-Pérez, A.J.; Camacho-López, M.A.; Morales-Luckie, R.A.; Sánchez-Mendieta, V. Structural evolution of Bi_2O_3 prepared by thermal oxidation of bismuth nano-particles. *Superf. y vacío* **2018**, *18*, 4–8.
30. *Diffra. Suite TOPAS*; Bruker AXS: Karlsruhe, Germany, 2015.
31. Li, P.; Chen, X.; Li, Y.; Schwank, J.W. A review on oxygen storage capacity of CeO_2 -based materials: Influence factors, measurement techniques, and applications in reactions related to catalytic automotive emissions control. *Catal. Today* **2019**, *327*, 90–115. [[CrossRef](#)]
32. Mehring, M. From molecules to bismuth oxide-based materials: Potential homo- and heterometallic precursors and model compounds. *Coord. Chem. Rev.* **2007**, *251*, 974–1006. [[CrossRef](#)]
33. Iyyapushpam, S.; Nishanthi, S.T.; Padiyan, D.P. Synthesis of β - Bi_2O_3 towards the application of photocatalytic degradation of methyl orange and its instability. *J. Phys. Chem. Solids* **2015**, *81*, 74–78. [[CrossRef](#)]

34. Shannon, R.D.; Prewitt, C.T. Effective ionic radii in oxides and fluorides. *Acta Crystallogr. Sect. B Struct. Crystallogr. Cryst. Chem.* **1969**, *25*, 925–946. [[CrossRef](#)]



© 2020 by the authors. Licensee MDPI, Basel, Switzerland. This article is an open access article distributed under the terms and conditions of the Creative Commons Attribution (CC BY) license (<http://creativecommons.org/licenses/by/4.0/>).